Experimental Eye Research 185 (2019) 107683

Contents lists available at ScienceDirect

Experimental Eye Research

journal homepage: www.elsevier.com/locate/yexer

Noninvasive imaging of the tree shrew eye: Wavefront analysis and retinal imaging with correlative histology

Benjamin S. Sajdak[a,b,c,1,2], Alexander E. Salmon[a,1], Jenna A. Cava[b], Kenneth P. Allen[d,e], Susan Freling[f], Ramkumar Ramamirtham[g,h], Thomas T. Norton[i], Austin Roorda[j], Joseph Carroll[a,b,*]

[a] Cell Biology, Neurobiology and Anatomy, Medical College of Wisconsin, Milwaukee, WI, United States
[b] Ophthalmology and Visual Sciences, Medical College of Wisconsin, Milwaukee, WI, United States
[c] Morgridge Institute for Research, Madison, WI, United States
[d] Biomedical Resource Center, Medical College of Wisconsin, Milwaukee, WI, United States
[e] Microbiology and Immunology, Medical College of Wisconsin, Milwaukee, WI, United States
[f] Max Planck Florida Institute for Neuroscience, Jupiter, FL, United States
[g] Ophthalmology, Boston Children's Hospital, Boston, MA, United States
[h] Harvard Medical School, Boston, MA, United States
[i] Optometry and Vision Science, University of Alabama at Birmingham, Birmingham, AL, United States
[j] School of Optometry and Vision Science Graduate Group, University of California Berkeley, Berkeley, CA, United States

ARTICLE INFO

Keywords:
Cone photoreceptors
Tree shrew
Adaptive optics
Optical coherence tomography
Megamitochondria

ABSTRACT

Tree shrews are small mammals with excellent vision and are closely related to primates. They have been used extensively as a model for studying refractive development, myopia, and central visual processing and are becoming an important model for vision research. Their cone dominant retina (~95% cones) provides a potential avenue to create new damage/disease models of human macular pathology and to monitor progression or treatment response. To continue the development of the tree shrew as an animal model, we provide here the first measurements of higher order aberrations along with adaptive optics scanning light ophthalmoscopy (AOSLO) images of the photoreceptor mosaic in the tree shrew retina. To compare intra-animal *in vivo* and *ex vivo* cone density measurements, the AOSLO images were matched to whole-mount immunofluorescence microscopy. Analysis of the tree shrew wavefront indicated that the optics are well-matched to the sampling of the cone mosaic and is consistent with the suggestion that juvenile tree shrews are nearly emmetropic (slightly hyperopic). Compared with *in vivo* measurements, consistently higher cone density was measured *ex vivo*, likely due to tissue shrinkage during histological processing. Tree shrews also possess massive mitochondria ("megamitochondria") in their cone inner segments, providing a natural model to assess how mitochondrial size affects *in vivo* retinal imagery. Intra-animal *in vivo* and *ex vivo* axial distance measurements were made in the outer retina with optical coherence tomography (OCT) and transmission electron microscopy (TEM), respectively, to determine the origin of sub-cellular cone reflectivity seen on OCT. These results demonstrate that these megamitochondria create an additional hyper-reflective outer retinal reflective band in OCT images. The ability to use noninvasive retinal imaging in tree shrews supports development of this species as a model of cone disorders.

1. Introduction

In humans, cone photoreceptors mediate high-spatial acuity and color vision and therefore represent a critical cell population for completing visual tasks and navigating our environment. Diseases that affect cone function have devastating effects on day-to-day life and

* Corresponding author. Department of Ophthalmology & Visual Sciences, Medical College of Wisconsin, 925 N 87th St, Milwaukee, WI, 53226-0509, United States.
E-mail address: jcarroll@mcw.edu (J. Carroll).
[1] BSS and AES contributed equally to the work presented here and should therefore be regarded as equivalent authors.
[2] Current affiliation: Morgridge Institute for Research, University of Wisconsin-Madison, Madison, WI, United States.

https://doi.org/10.1016/j.exer.2019.05.023
Received 7 April 2019; Received in revised form 21 May 2019; Accepted 28 May 2019
Available online 31 May 2019
0014-4835/ © 2019 Elsevier Ltd. All rights reserved.

Abbreviations:

AOSLO	adaptive optics scanning light ophthalmoscopy
FWHM	full-width half-max
HORMS	high-order root mean square
LCA	longitudinal chromatic aberration
LRP	longitudinal reflectance profile
MTF	modulation transfer function
OCT	optical coherence tomography
ONH	optic nerve head
PSF	point spread function
ROI	region of interest
SHWS	Shack-Hartmann wavefront sensor
TEM	transmission electron microscopy

represent a significant societal burden. Recently, exciting progress has been made in developing mammalian models to study mechanisms of cone disorders through inherited cone dystrophies (Kostic and Arsenijevic, 2016).[3] Due to their genetic malleability, much of this work is being done in nocturnal mice and rats (Slijkerman et al., 2015) who have poor vision and sparse cones. Non-human primates in the Infraorder *Simiiformes* (*e.g.* Marmoset and Macaque) offer a comparable representation of the human fovea, but high per-animal cost, ethical concerns, and low availability are limitations that most research institutions cannot overcome. Large animal models with a "fovea-like" area centralis (*e.g.* dogs (Beltran et al., 2014) and pigs (Hendrickson and Hicks, 2002; Kaplan et al., 2017)) are appealing because of lower costs and higher availability, but their size and maintenance makes experimental logistics challenging so they are used in relatively few labs.

Noninvasive retinal imaging has provided a solution to one of the limitations associated with alternative animal models: low availability. The ability to conduct a longitudinal imaging study maintains statistical power while reducing the required number of animals. However, retinal imaging involving large animal models can present significant logistical and engineering challenges. Despite the many advancements balancing practicality and relevance in animal modeling, a critical research gap remains between nocturnal rodents and large animal work, further motivating the development of cone dominant small mammalian models for vision research.

Diurnal rodents strike a balance between relevance to cone disorders and logistics. While no rodent model can fully represent the human retina, Nile rats and ground squirrels have cone-rich retinal regions (Bobu et al., 2006; Kryger et al., 1998) and photoreceptor transcriptomes that may be more relevant to cone retinopathies than natural and genetically modified nocturnal species (Mustafi et al., 2016). The guinea pig has been shown to serve as a useful model for refractive development (McFadden et al., 2004), but does not exhibit a preponderance of cones (Peichl and Gonzalez-Soriano, 1994). Recent studies using the 13-lined ground squirrel have led to new insights into cone biology (Beier et al., 2018; Kiser et al., 2018; Mustafi et al., 2016) and this species is amenable to *in vivo* retinal imaging (Sajdak et al., 2016, 2018). However, this species of ground squirrel is an obligate hibernator, and its retina undergoes reversible structural and transcriptomic remodeling throughout hibernation (Kuwabara, 1975; Luan et al., 2017; Mehta et al., 2013; Merriman et al., 2016; Remé and Young, 1977), and therefore offers a limited annual window in which to study a physiologically consistent homeothermic retina.

Northern tree shrews (*Tupaia belangeri*) are small mammals (~200 g) that are closely related to primates (order *Scandentia*). They have a substantial binocular visual field (Fig. 1A), (Kaas et al., 1972) and demonstrate complex visual and social behaviors (Emmons, 2000; Mustafar et al., 2018). The visual pathways and primary visual cortex are highly developed (Lund et al., 1985). The tree shrew retina contains ~95% cones comprised of short wavelength-sensitive cones (S-cones) and long wavelength-sensitive cones (L-cones) in a ratio of 1:12.6) (Müller and Peichl, 1989). Accordingly, tree shrews have been shown to be dichromats with a neutral point of approximately 504 nm (Jacobs and Neitz, 1986). The value of tree shrews as an intermediary species between primate and rodent has been leveraged in studies of postnatal refractive development, the emmetropization mechanism, and in studies of visual system anatomy and neurophysiology (Lee et al., 2016; Norton and McBrien, 1992; Sesma et al., 1984; Usrey et al., 1992).

Although *in vivo* retinal assessment of this species has been limited, recent studies have utilized optical coherence tomography (OCT) of the retina to study histological correlations (Abbott et al., 2009), retinal thinning in myopia (Abbott et al., 2011), inner retina optophysiology (Erchova et al., 2018), and to assess the lamina cribrosa and retinal nerve fiber layer in a model of glaucoma (Samuels et al., 2018). The cone inner segments of the tree shrew contain mitochondria that are much larger than in other species (termed "megamitochondria") (Knabe et al., 1997; Samorajski et al., 1966). This feature may be of particular

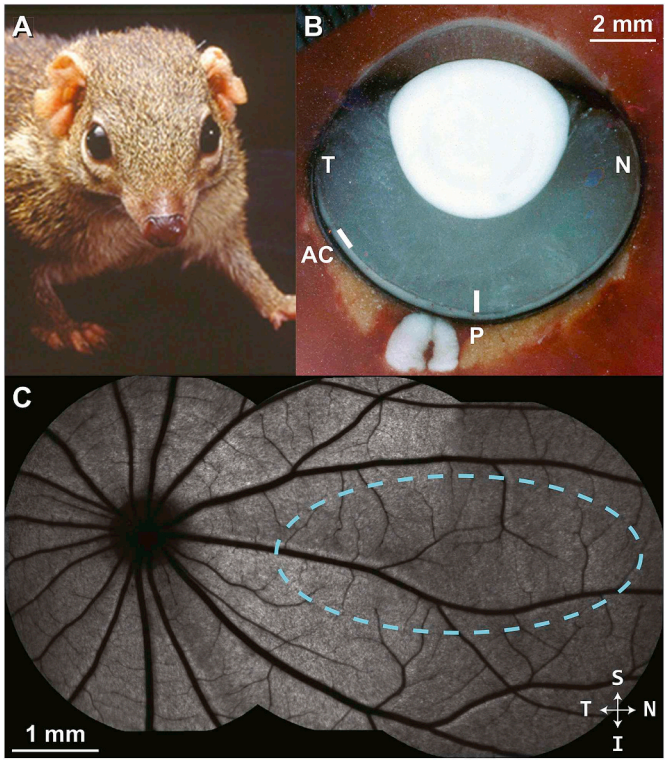

Fig. 1. Tree shrew ocular anatomy overview. (A) A northern tree shrew showing laterally-placed eyes and binocular visual field. (B) Horizontal section through a flash-frozen tree shrew right eye. N = nasal; T = temporal; P = approximate posterior pole; AC = approximate location of area centralis. In contrast to primates, the optic disc is located in the temporal retina; the posterior pole region is nasal to the optic disc. (C) A montage of blue autofluorescence images in the tree shrew retina indicating the vascular pattern radiating outward from the optic disc. In this study, cardinal axes (superior/inferior, nasal/temporal) were defined relative to the ONH, as it was the most distinct retinal feature. *Dashed cyan outline* = approximate visual streak (Müller and Peichl, 1989). (For interpretation of the references to color in this figure legend, the reader is referred to the Web version of this article.)

[3] Extensive research into cone biology and refractive development has also been conducted in (but not limited to) zebrafish (Link and Collery, 2015) and chick (Wisely et al., 2017); however the scope of this study and discussion will be limited to mammalian models.

interest, as the mitochondria are thought to be the source of some of the hyper-reflective outer retinal bands seen on OCT images (Spaide and Curcio, 2011). Tree shrews have approximately the same numerical aperture as mice (Callahan and Petry, 2000; Geng et al., 2011; Norton and McBrien, 1992), resulting in an excellent theoretical lateral resolution with AOSLO (< 1 μm).

To provide additional information that may foster ophthalmic research using tree shrews, we have analyzed the optical performance of the tree shrew eye, demonstrated noninvasive retinal imaging techniques in the tree shrew including OCT and AOSLO, and compared our *in vivo* measurements to those obtained *ex vivo* using confocal and electron microscopy.

2. Methods

2.1. Animals

As listed in Supplementary Table 1, measurements were made on 10 juvenile and young adult northern tree shrews (*Tupaia belangeri*) at the University of Alabama at Birmingham (UAB) and at the Medical College of Wisconsin (MCW). The animals at UAB were raised by their mothers in the UAB Tree Shrew Core. Animals measured at MCW were obtained after weaning from the Max Planck Florida Institute for Neuroscience. The experimental procedures at both UAB and MCW were conducted in accordance with the ARVO Statement for the Use of Animals in Ophthalmic and Vision Research, occurred in AAALAC international-approved animal research facilities, and were approved by the Institutional Animal Care and Use Committees at each institution.

2.2. Refraction and wave aberration measurements

Refractive and wavefront measurements were conducted on 7 juvenile tree shrews (11 eyes) at similar ages to the animals used for retinal imaging (Supplementary Table 1). All animals had previously received a dental acrylic pedestal placed atop the skull while under anesthesia (100 mg/kg ketamine, 7.0 mg/kg xylazine, i.m.) as described by (Siegwart and Norton, 1994). All measurements were made in awake animals either with 1% atropine cycloplegia or without cycloplegia.

Refractive measurements were obtained in awake animals with a Nidek ARK-700 autorefractor as reported previously (Norton et al., 2010). The animals were gently restrained while 5 autorefractor measurements were obtained for each eye. These measurements were averaged, converted to spherical equivalent at the corneal plane, and adjusted for the small-eye artifact of retinoscopy (Glickstein and Millodot, 1970), by subtracting 4 diopters (D) of apparent hyperopia from the autorefractor measurements (Norton et al., 2003).

For the wavefront measurements, each animal was placed in a Plexiglas restraint tube for less than 1 h as described previously (Norton et al., 2006). Ventilation holes prevented build-up of body heat. The tube was mounted on a photographic tripod and the animal's head was held in a comfortable position with a clip attached to the dental acrylic pedestal. The eye was aligned with the wavefront apparatus to make measurements perpendicular to the pupil plane (Fig. 1B). The animals blinked as needed, generally made only very small eye movements, and showed no signs of distress during the measurement session.

Wavefront aberration measurements were made with a custom-built Shack-Hartmann wavefront sensor (SHWS) (Liang and Williams, 1997). In 5 eyes of 3 animals, measurements were made with atropine cycloplegia. In 6 eyes of 4 animals, the measurements were made without cycloplegia in dim room illumination which dilated the pupils. In this system, 840 nm light from a superluminscent diode was collimated, narrowed to < 1 mm diameter, and directed into the eye of the tree shrew. The average power of the beam was ~10 μW. The back-scattered light was passed through an afocal *4f* telescope assembly to relay the image of the tree shrew's pupil with a magnification of 1.6x onto a rectangular lenslet array (400 μm spacing, 24 mm focal length) with an effective lenslet sampling of 250 μm.

Five SHWS images, each with an exposure time of 100 ms, were taken along the optical axis for each eye. The three best images were selected and analyzed with custom software. In all images, two overlapping spot patterns of different sizes were observed (Supplementary Fig. 1A). We surmised that these spot patterns arose from the two dominant scattering surfaces in the retina, with the wider spaced pattern (more hyperopic) arising from the nerve fiber layer and the smaller pattern (relatively less hyperopic) arising from the photoreceptors (Supplementary Fig. 1B). We took care to select and analyze the spots originating from the photoreceptor layer (Supplementary Fig. 1C). Wavefront aberrations were measured over a 4 mm pupil and were fit with a 6th order Zernike polynomial ordered according to the Optical Society of America standard (Thibos et al., 2002). The Zernike polynomial coefficients from the three best images from each animal were averaged together for further analysis. Computations of image quality metrics (point spread function (PSF), modulation transfer function (MTF), and depth of focus) employed all coefficients of the Zernike polynomial except defocus. Astigmatism was considered equally along with the high order aberrations. These data were compared to a previously reported human dataset (Cheng et al., 2004) for which the Zernike coefficients that describe the wavefronts were recomputed for a 4 mm pupil using algorithms described previously (Lundstrom and Unsbo, 2007).

Owing to the fact that tree shrew aberrations are relatively high compared to human, we found that conventional approaches to estimate the refractive error of the eye based on wavefront aberrations were either unreliable (computing directly from the Zernike defocus coefficient) or noisy (computing refractive error as the defocus where the Strehl ratio peaks). Additionally, we wanted to compute the refractive error by finding a defocus setting that optimized an image quality metric that was more suited to the visual capabilities of the tree shrew. As such, we estimated refractive error as the defocus setting that yielded the highest contrast of a checkerboard pattern with a check size of 21 arcmin, corresponding to a fundamental spatial frequency of 1.4 cyc/deg – higher than the peak sensitivity, but below the functional spatial frequency cut-off of a tree shrew (Petry et al., 1984). The checkerboard pattern also mimicked the experimental approach used by Norton et al. (2003) for functional estimates of refractive error. We used the same stimulus to quantify the depth of focus of the eye, by computing the range over which the contrast was within ½ of the peak contrast (full-width half-max; FWHM). Finally, refractive errors were corrected for the longitudinal chromatic aberration (LCA) between 840 and 550 nm. To estimate LCA of the tree shrew eye, we developed a single refracting surface eye model (Hughes, 1979) using schematic eye parameters from Norton and McBrien (1992) and computed powers at different wavelengths using model equations for the refractive index of water as a function of wavelength (Huibers, 1997; Quan and Fry, 1995). LCA between the measurement wavelength of 840 nm and 550 nm was ~4.5D.

2.3. Anesthesia and preparation for retinal imaging

Animals used for retinal imaging are shown in Supplementary Table 1. Animals were anesthetized with inhaled isoflurane (5% induction, 1–4% maintained by nose-cone) in 1 L/min 100% oxygen flow using a non-rebreathing system (VetEquip, Inc., Livermore, CA, USA), placed on a heated rodent alignment stage with two rotational and three translational degrees of freedom. One drop each of 1% tropicamide and 2.5% phenylephrine (Akorn, Inc., Lake Forest, IL, USA) was applied to the eye to induce dilation and cycloplegia. A bent pediatric ocular speculum was used to keep the eyelids open and wetting drops were applied as needed (about every 2 min) to maintain corneal hydration. This species occasionally stops breathing under isoflurane anesthesia (common in 1/3 tree shrews in this study), so the animal's respiratory rate was constantly monitored by a dedicated researcher to

adjust or stop isoflurane flow as needed. Imaging and euthanasia were performed under anesthesia between the hours of 10AM-3PM. Imaging sessions under anesthesia often lasted up to an hour; during this time, none of the tree shrews developed transient cataracts.

2.4. Confocal scanning light ophthalmoscopy (cSLO)

Retinas were imaged using a custom multiline cSLO (modified Spectralis HRA; Heidelberg Engineering, Heidelberg, Germany) and the mouse lens. Near-infrared (820 nm) reflectance and blue auto-fluorescence (486 nm excitation with 502–537 nm band pass emission) imaging was performed. Automatic real-time tracking in the Spectralis software (HRA2/Spectralis Family Acquisition Module ver. 6.5.2.0) was used to register and average 50–80 frames. Images were montaged using i2k Retina (DualAlign LLC, Clifton Park, NY, USA) with quadratic transformations to account for the spherical warping inherent in wide-field retinal imaging.

2.5. Optical coherence tomography (OCT)

Imaging was performed with a Bioptigen Envisu R2200 Spectral Domain OCT system (Leica Microsystems, Wetzlar, Germany) equipped with a Superlum Broadlighter T870 light source (central wavelength: 878.4 nm, bandwidth: 186.3 nm; Superlum, Cork, Ireland). Bioptigen's Rabbit lens was used for retinal imaging.

Horizontal and vertical line scans (650 A-scans/B-scan; 100 repeated B-scans) of the retina were acquired near the posterior pole, nasal to optic nerve head (ONH) which was visible in each scan as a landmark (Fig. 1B and C). As in the first report of tree shrew OCT (Abbott et al., 2009), due to positional constraints caused by our anesthesia nosecone and the long nose of the tree shrew, we were unable to image the area centralis which is located in the temporal retina, about 30° from the ora serrata (Fig. 1B) (Müller and Peichl, 1989). Thus, these images were taken in the posterior pole region, nasal to the ONH as were the wavefront measurements. Fifty B-scans were registered (allowing translation only) to a manually chosen reference frame and averaged using the TurboReg plugin in ImageJ (National Institutes of Health, Bethesda, MD) (Schneider et al., 2012; Thévenaz et al., 1998). Custom software (OCT Reflectivity Analytics; github.com/whytestalyon/ORA) was then used to measure retinal layer thickness or distances between outer retinal hyper-reflective bands from the linear image (Wilk et al., 2017). Ten 5-pixel-wide longitudinal reflectance profiles (LRPs) were collected from the nasal retina near the posterior pole (5 LRPs each from the horizontal and vertical line scan) for peak-to-peak and FWHM measurements. We used the following Band 1–4 (B1-4) assignments for outer retinal bands: B1 as the anatomic external limiting membrane (ELM), B1.5 as the signal seen in between established B1 and B2, B2 as either the ellipsoid zone or inner segment/outer segment junction, B3 as the interdigitation zone or outer segment tips, and B4 as the retinal pigmented epithelium (RPE)-basal lamina-Bruch's membrane (Fig. 6). Volume scans were nominally 8 × 8mm with isotropic sampling (650 A-scans/B-scan; 650 B-scans).

2.6. Adaptive optics scanning light ophthalmoscopy (AOSLO)

Images of the cone mosaic were acquired using a custom AOSLO modified for a 4.5 mm pupil diameter at retinal locations comparable to the OCT measurements. Confocal and non-confocal split-detection images were recorded simultaneously (Scoles et al., 2014). Images were collected at the optic nerve for spatial alignment to cSLO, and photoreceptor images were recorded ~30–45° (2–3 mm) nasally from the optic nerve near the posterior pole (this location corresponds to the approximate optic axis of the tree shrew eye). Sinusoidal distortion inherent in our scanning system was estimated by imaging a Ronchi grating with 3000 cycles/inch, then corrected by resampling the video frames over a grid of equally spaced pixels. The scale of the AOSLO images (in μm/pixel) was determined by calculating the degrees/pixel in the resampled image of the Ronchi grating, then multiplying by the tree shrew retinal magnification factor (76μm/degree; based on the 4.35 mm posterior nodal distance of the species (Callahan and Petry, 2000)), before scaling linearly by the ratio of the animal's axial length (measured by digital caliper after enucleation; Mitutoyo, Takatsu-ku, Japan) and a reference axial length of 8.06 mm (mean adult tree shrew axial length (Norton and McBrien, 1992)).

Reference frames were automatically selected (Salmon et al., 2017), then 50 images were registered and averaged (Dubra and Harvey, 2010). The resulting images were automatically montaged with custom software (Chen et al., 2016). 55 × 55 μm or 100 × 100 μm regions of interest (ROIs) were selected from split-detector AOSLO images for cone mosaic analysis using custom software (Translational Imaging Innovations, Inc.). Cones were semi-automatically identified using a segmentation method designed for split detector AOSLO images (Cunefare et al., 2016). Cone density, spacing, and Voronoi geometry were derived from the cone coordinates as previously described (Cooper et al., 2016).

2.7. Tissue preparation and histology

Two of the tree shrews (TS1 and TS2) were euthanized under anesthesia by intraperitoneal injection of a pentobarbital-based euthanasia solution (Euthasol, Virbac, Carros, France) for subsequent histologic analysis. Eyes were then enucleated, and approximate axial length was measured with a digital caliper (eyes were not inflated to re-approximate normal intraocular pressure).

Right eyes were immersion fixed overnight in 4% paraformaldehyde (PFA) in phosphate-buffered saline (PBS) at 4 °C for whole-mount immunocytochemistry. Whole globes were rinsed 3 times for 5 min in PBS and the cornea and lens were removed. Eye cups were permeabilized with Proteinase K (20 μg/ml diluted in PBS) for 30 min at room temperature and rinsed again in PBS. Permeabilization was stopped with 4% PFA for 30 min, and eye cups were rinsed in PBS. The sclera, optic nerve, and choroid were then carefully removed from the retina. The RPE remained across most of the whole-mount, only being easily detached in a few regions. Retinas were then incubated for 60 min at room temperature in a blocking solution (2% goat serum. 1% Triton X-100, and 1% Tween-20 in PBS). Retinas were incubated under gentle rocking at room temperature for 24 h in a blocking solution with primary antisera. L- and S-opsin were detected with chicken antiserum JH 6105 and rabbit antiserum JH 455 (each diluted 1:100 in blocking buffer), respectively. Retinas were rinsed under gentle rocking at room temperature 3 times for 60 min in 1% Tween-20 in PBS. Primary antibody binding was then detected with anti-chicken and anti-rabbit secondary antisera (each diluted 1:500 in 1% Tween-20 in PBS) at 4 °C for 24 h. Retinas were rinsed 4 times for 30 min in 1% Tween-20 in PBS, then 5–6 radial cuts were made in the peripheral retina to flat-mount the retina photoreceptor-side up for immunofluorescence imaging. Confocal immunofluorescence images of flat-mounted retina were captured with an Olympus VS120 virtual slide microscope (Olympus, Tokyo, Japan) and bright-field images were captured with a Leica DM IL LED inverted microscope (Leica Microsystems, Wetzlar, Germany).

The inner retina was also imaged with an inverted microscope to obtain the vascular pattern of TS1 and TS2 to allow retinal imaging and histological multi-modal alignment to assess cone densities at approximately the same retinal region *in vivo* and *ex vivo*. Once aligned, 100 × 100μm ROIs were selected using custom software (Translational Imaging Innovations, Inc.). A topography map from the right eye of TS1 was generated as described previously (Cohn et al., 2015), using density values from 63 ROIs sampled every 1 mm. Four additional 200 × 200μm ROIs were collected 2 mm superior, inferior, temporal, and nasal (near the optic axis) from the optic nerve head from each

whole-mount for cone ratio analysis. These images were converted to grayscale for semi-automated cone detection and subsequent density, percent six-sided Voronoi, nearest neighbor distance, and density recovery profile distance measurements (Rodieck, 1991; Roorda et al., 2001).

Left eyes were processed for electron microscopy as described previously (Sajdak et al., 2018). In brief, whole globes were immersion fixed overnight in 2% PFA, 2% glutaraldehyde in 0.1 M cacodylate buffer. The cornea and lens were removed, and retinal regions imaged *in vivo* were dissected from the eye cup and post-fixed in 1% osmium tetroxide followed by dehydration in a graded methanol series, then infusion with acetonitrile, and embedded in epoxy resin. Once the epoxy molds solidified, 500 nm sections were cut and stained with 1% toluidine blue to ensure that cones were visible in vertical cross-sectional (or horizontal *en face*) orientation. Once the epoxy molds were sectioned in the correct plane, 70 nm sections were cut, collected onto hexagonal grids, and stained with uranyl acetate and lead citrate for transmission electron microscopy (TEM). Axial distances of the following cone structures were then measured from vertically oriented cones: inner segment myoid (ISm), inner segment ellipsoid (ISe), outer segment (OS), and RPE.

2.8. Statistics

All statistical tests were performed using Prism version 7.04 (GraphPad, LaJolla, CA) or Matlab 2017b (Math-Works, Inc., Natick, MA) with the Statistics and Machine Learning Toolbox ver. 11.2. Intra-animal *in vivo* and *ex vivo* cone mosaic density and cell spacing were tested for normality using D'Agostino & Pearson tests. Wilcoxon matched-pairs tests were used on these nonparametric paired data. Chi-square tests were used to compare cone packing geometry of L- and S-cones.

3. Results

3.1. Wavefront aberrations

The mean and standard deviation of the Zernike coefficient values for all 11 eyes over a 4 mm pupil are shown in Fig. 2A and B. Defocus is by far dominant, and is hyperopic, due primarily to the 4.5D of LCA of the eye (Fig. 2A), compared to the higher order aberrations which show no tendencies in any specific directions (Fig. 2B). Fig. 2C plots the magnitude of aberrations for different collections of Zernike terms. The aberration is dominated by 2nd order Zernike terms with defocus being the most dominant term. As is typical for ocular wave aberrations, the RMS error decreases with increasing order (Porter et al., 2001). High-order RMS (HORMS) was 0.44 μm, 3.7 times higher than the humans in our comparison dataset for the same pupil size (HORMS = 0.12 μm). HORMS + Astigmatism, which comprise the terms used for image quality metric calculations, was 0.65 μm. MTFs were computed at the defocus with the highest contrast of the checkerboard pattern for each eye (Fig. 2D).

3.2. Refractive error and depth of focus

Table 1 shows the refractive error and depth of focus estimates for the 11 eyes. The Shack-Hartmann estimated refractive error (0.71 ± 0.61 D) and the corrected Nidek autorefractor measurements (1.01 ± 0.51 D) both indicated that young tree shrews are slightly hyperopic, as suggested by previous reports (Gawne et al., 2018; Norton et al., 2003).

3.3. Noninvasive assessment of the tree shrew Retina

We obtained cSLO, OCT, and AOSLO images from 3 adult tree shrews. Using the ONH and nasal vasculature as landmarks, we aligned

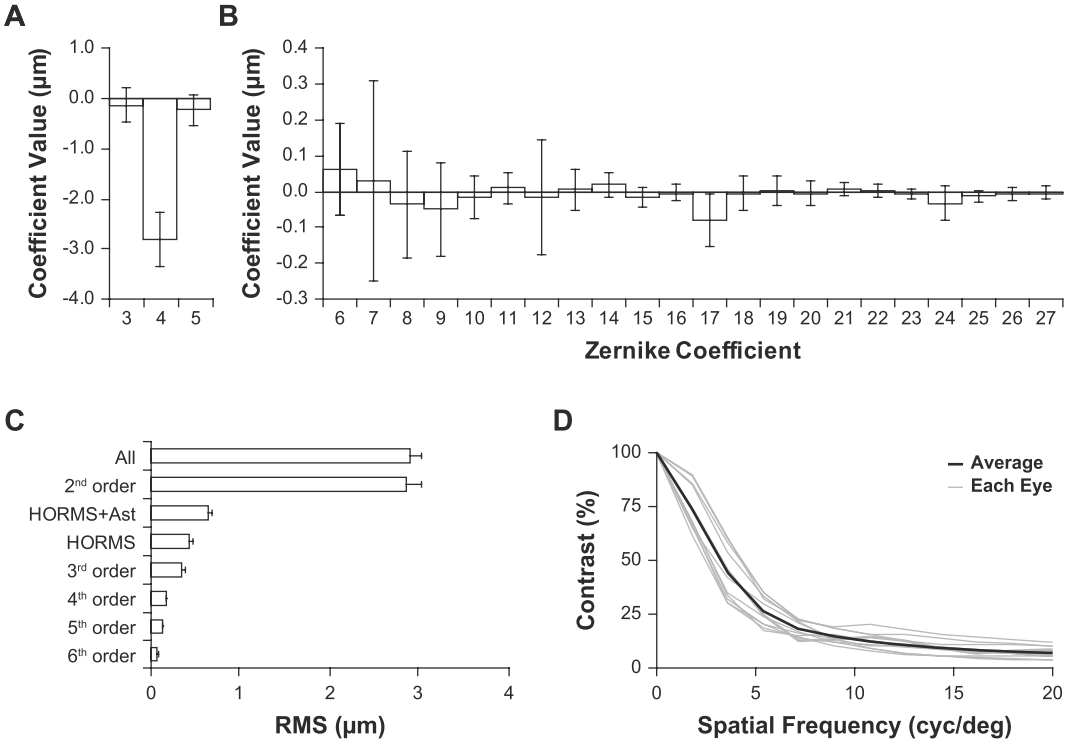

Fig. 2. Wavefront analysis of the tree shrew eye perpendicular to the pupil plane. (A–B) Contribution of Zernike coefficients (The Optical Society of America single index notation) to tree shrew wavefront error. The primary contributor is defocus (A), plots are scaled differently to better visualize HORMS (B). (C) Summary of the contribution of Zernike terms to wavefront RMS. (D) Radially-averaged MTF computed at the defocus level that maximized contrast of a 21 arcmin checkerboard stimulus. (A–D) Pupil size: 4 mm; n = 11 eyes. (A–C) Data are expressed as mean ± SD.

Table 1
Wave aberration and refraction data.

ID, Eye	Refraction (NIDEK; D)	Refraction (SHWS; D)	SHWS-NIDEK (D)	Depth of focus (SHWS; D)	HORMS (μm)	HORMS + AST (μm)
216OS	1.08[a]	0.13[a]	−0.95	4.40	0.37	0.40
246OD	1.53	0.88[a]	–	4.80	0.43	0.57
246OS	0.85	0.09[a]	–	4.60	0.41	0.47
259OD	1.29	0.14[a]	–	3.40	0.45	0.68
259OS	0.38	−0.21[a]	–	5.00	0.53	1.00
261OS	2.03[a]	0.76[a]	−1.27	5.00	0.51	0.76
263OD	0.79	1.11	0.32	4.60	0.50	0.76
264OD	1.46	1.59	0.13	5.20	0.38	0.67
264OS	1.72	1.05	−0.67	5.00	0.36	0.59
265OD	0.64	0.65	0.01	4.40	0.37	0.47
265OS	1.38	1.61	0.23	5.60	0.47	0.79
Mean	**1.01**	**0.71**	**−0.41**	**4.73**	**0.44**	**0.65**
SD	**0.51**	**0.61**	**0.65**	**0.57**	**0.06**	**0.17**

[a] Indicates measurements made with atropine cycloplegia. Difference between autorefractor and wavefront measurements of refraction was calculated only for eyes in which both were measured with, or without cycloplegia because cycloplegia causes a small hyperopic shift. SHWS-based refraction and depth of focus estimates used the maximum contrast of the 21 arcmin checkerboard stimulus and were corrected for LCA.

retinal cross-sections revealed with OCT and the photoreceptor mosaic revealed with AOSLO to the *en face* cSLO (Fig. 3). Cones comprise about 94–98% of all photoreceptors in the nasal and superior retinal locations imaged with AOSLO in this study (Müller and Peichl, 1989; Petry et al., 1993). The large size of the cones (~6 μm) in tandem with the high resolution of our AOSLO system (~1.0 μm in this species) reveals a variety of reflectivity patterns with confocal AOSLO (Fig. 3C). This appearance seen with confocal AOSLO complicates the use of conventional, local maximum-based cone detection schemes (Li and Roorda, 2007), resulting in multiple false positives that may change with repeat imaging (Cooper et al., 2011). This suggests that confocal AOSLO may not be sufficient to reliably track individual cones in the tree shrew retina, but that split-detector AOSLO offers a possible solution. When present and reflective, the sporadic rod was visible with confocal and split-detection AOSLO (Fig. 3C).

With AOSLO, we found that cone density is relatively uniform along the horizontal meridian nasally from the ONH (Fig. 4A; $p = 0.09$, linear regression), but there is a significant decrease in density with distance superior from the horizontal meridian (Fig. 4B; $p = 3.51_E{}^{-5}$, linear regression). Example confocal and split-detector images from areas of low and high density are given in Fig. 4C. The AOSLO data agree well with a topographical map of cone density generated from cone coordinates identified on immunofluorescence images from a whole-mounted retina (Fig. 4D). The inter-cone spacing ranges from the AOSLO images was 5.7–6.3 μm along the horizontal meridian, and 5.6–6.8 μm in the vertical meridian, which compares well to the cone spacing of 6 μm "in the central retina" in a previous topography characterization of this species (Müller and Peichl, 1989).

3.4. Comparing in vivo and ex vivo cone density

To assess how *in vivo* (AOSLO) and *ex vivo* (whole-mount) cone densities compared in the same animal, we measured regions equidistant from the ONH along the horizontal meridian. As expected, cone density was significantly higher in the whole-mount ROIs (Fig. 5B) compared to the AOSLO ROIs (Fig. 5A) in both animals (TS1 AOSLO = 31,283 ± 2493 cones/mm^2 vs TS1 whole-mount = 34,201 ± 3280 cones/mm^2, $p = 0.0039$, Wilcoxon matched-pairs signed rank test; TS2 AOSLO = 32,959 ± 545 cones/mm^2 vs TS2 whole-mount = 39,115 ± 2304 cones/mm^2, $p = 0.0020$, Wilcoxon matched-pairs signed rank test). A tissue shrinkage factor of 4.50% was derived from the average ratio of nearest-neighbor distances between AOSLO and whole-mount for these two animals but was as high as 12% in the nasal periphery of TS2. Cone density would be expected to increase by the square of this linear shrinkage factor (Fig. 5C).

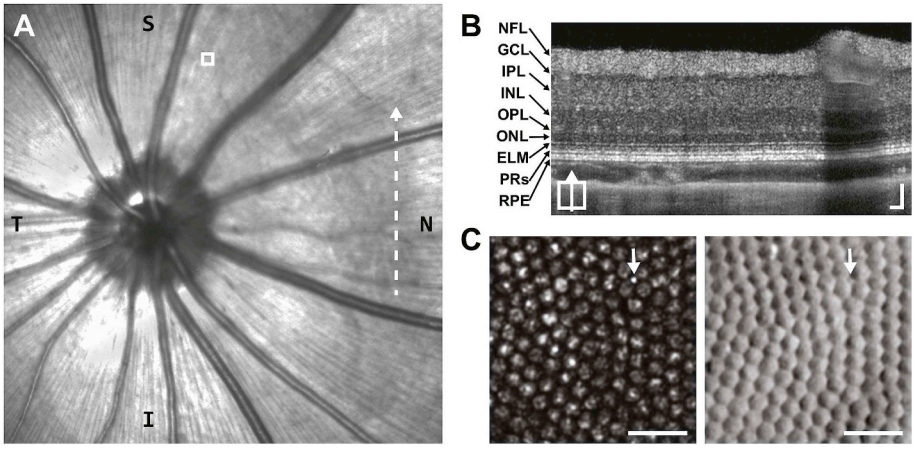

Fig. 3. Example of *in vivo* images from tree shrew retina (right eye). (A) Near-infrared confocal scanning light ophthalmoscope fundus image including optic nerve head. T = temporal; N = nasal; S = superior; I = inferior. *Dashed-line* indicates position of (B). *White box* indicates AOSLO region shown in (C). (B) Tree Shrew retinal layers visualized with a vertical B-scan OCT captured from the posterior pole region nasal to the optic disc (Supplementary Fig. 1). NFL = nerve fiber layer; GCL = ganglion cell layer; IPL = inner plexiform layer; INL = inner nuclear layer; OPL = outer plexiform layer; ONL = outer nuclear layer; ELM = external limiting membrane; PRs = photoreceptors; RPE = retinal pigmented epithelium. Scale bars = 50 μm. (C) Tree shrew photoreceptor mosaic images captured simultaneously with confocal (left) and split-detection (right) AOSLO. Note the multiple reflectance peaks per cone on confocal, but unambiguous cone boundaries on split-detection. The arrows point out the presumed lone rod in this region. Scale bars = 20 μm.

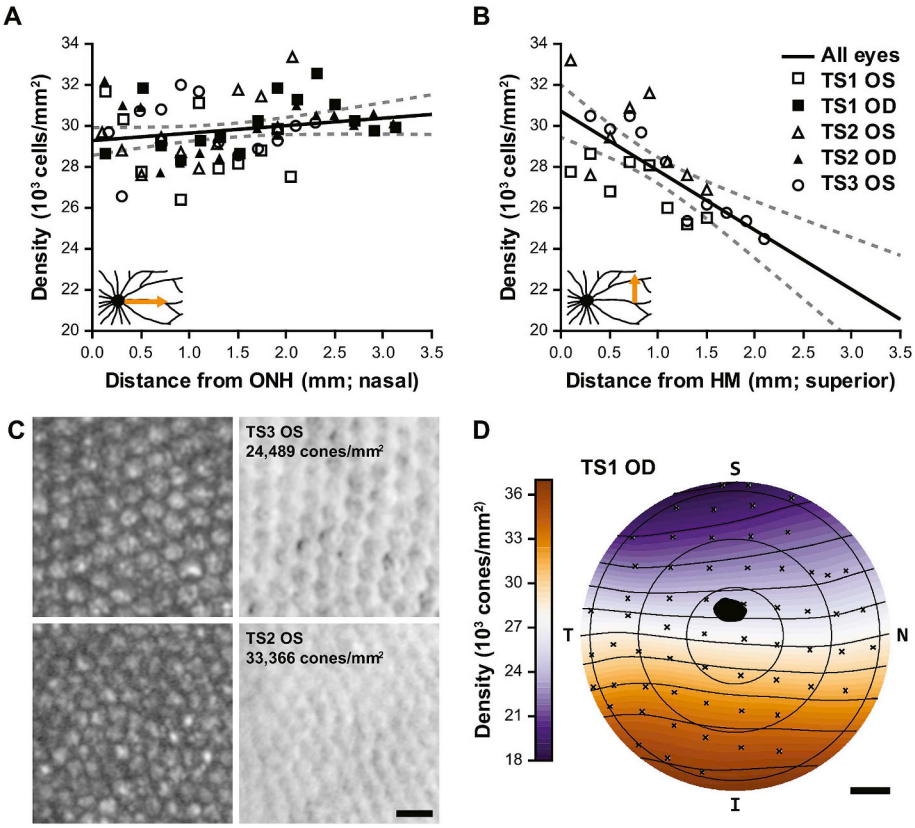

Fig. 4. Cone photoreceptor topography. (A–B) Cone densities measured with AOSLO as a function of eccentricity from the optic nerve head (ONH; A) and the approximate horizontal meridian (HM; B). *Solid black line*: linear regression of measurements for all eyes, *dashed lines*: 95% CI. Regression analysis did not indicate a significant change in density with nasal eccentricity (A; $p = 0.09$) but did indicate a significant decrease in density with superior eccentricity (B; $m = -2.91_E{}^3$cells/mm^2/mm; $p = 3.51_E{}^{-5}$). Insets show the schematized retinal regions that correspond to these data. (C) The top panels are the lowest density region analyzed in (A–B); the bottom panels are the highest density region (left and right are confocal and split-detector AOSLO, respectively). Scale bar = 10 µm. The trends in (A–B) correspond well with the topographical map generated from the TS1 OD whole-mount, (D) which demonstrates an overall density gradient decreasing superiorly. The black spot represents the ONH, S = superior; N = nasal; I = inferior; T = temporal; scale bar = 1 mm.

3.5. Ex vivo cone ratio and packing

Split-detection AOSLO is currently unable to identify cone type. Therefore, we assessed 4 ROIs (2 mm superior, inferior, temporal, and nasal from the ONH) from TS1 and TS2 whole-mounted retinas to assess cone ratio and packing. Percentage of S-cones from the regions sampled ranged from 5.4 to 8.3%, which is within the 4–10% range reported in the topographical characterization of this species (Müller and Peichl, 1989). Nearest-neighbor distance (any cone type) was similar across regions analyzed (5.04 ± 0.5 µm) compared to 18.79 ± 2.92 µm for the S-cone mosaic alone. Density recovery profile distance was also similar across regions analyzed (5.93 ± 0.6 µm). Supplementary Fig. 2 shows an example ROI with individual cones marked and the resulting packing geometry. The cone mosaic showed mostly triangular packing geometry across all eight 200 × 200µm ROIs sampled, with 82.14 ± 4.38% of all cones having 6-sided Voronoi domains. S-cones showed similar packing geometry compared to L-cones, with no significant difference in the proportion of 6-sided compared to non-6-sided cells ($p = 0.35$, Chi-square test).

3.6. Comparing in vivo and ex vivo cross-sections of outer Retina

To assess how the hyper-reflective bands in the outer retina compared to cone structure, we quantified peak-to-peak distances and the FWHM of OCT local maxima, and then lengths of subcellular structures on electron micrographs (Fig. 6). We reasoned that the tree shrew's megamitochondria might provide a stronger signal to assess the anatomical origins of B1.5 (initially seen in ground squirrel (Sajdak et al., 2018)) and B2. The distances between ELM to BrM and B1 to B4 were more similar for TS2 (30.7 ± 0.3 µm [OCT] vs. 31.5 ± 1.2 µm [EM]) than TS1 (30.6 ± 1.5 µm [OCT] vs. 35.6 ± 1.4 µm [EM]), suggesting variable effects of histological processing. When the ELM to BrM distances were normalized to the B1 to B4 axial distances, the junction of the ISm and ISe aligned with B1.5, and the junction of the ISe and outer segment aligned with B2. While the length of the ISe was comparable to the distance between B1.5 and B2 (Fig. 6C), the OCT FWHM of B2 was much smaller than the anatomical size of the ISe for both animals used in these comparisons: TS1 B2 FWHM = 3.4 ± 0.5 µm, and TS1 ISe = 11.9 ± 0.8 µm; TS2 B2 FWHM = 3.6 ± 0.5 µm, and TS2

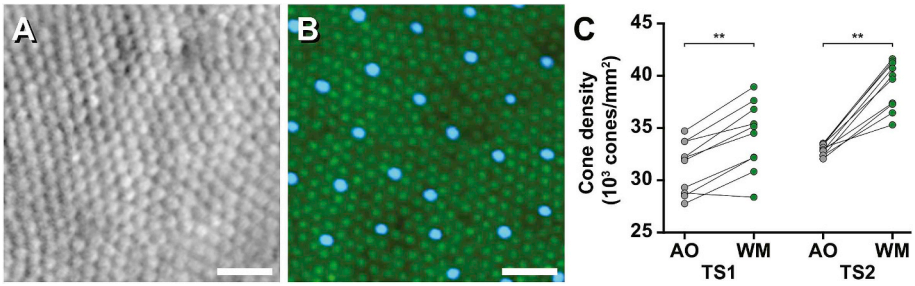

Fig. 5. Intra-animal comparison of tree shrew cone density from ROIs captured at the same eccentricity relative the optic nerve *in vivo* and *ex vivo*. Split detector AOSLO image (A) and whole-mount (WM) immunofluorescent image with L-opsin (green) and S-opsin (blue) (B) both 2.3 mm nasal from the ONH of TS2. (A & B) In this example, the *in vivo* density from AOSLO (33,491 cones/mm^2) is lower than the *ex vivo* density from the whole-mounted retina (41,275 cones/mm^2). Scale bars = 20 µm. AOSLO (AO) cone densities were significantly lower compared to WM cone densities from locations equidistant from the ONH for both TS1 and TS2 (C). **P < 0.01, Wilcoxon match-pairs signed ranks test. (For interpretation of the references to color in this figure legend, the reader is referred to the Web version of this article.)

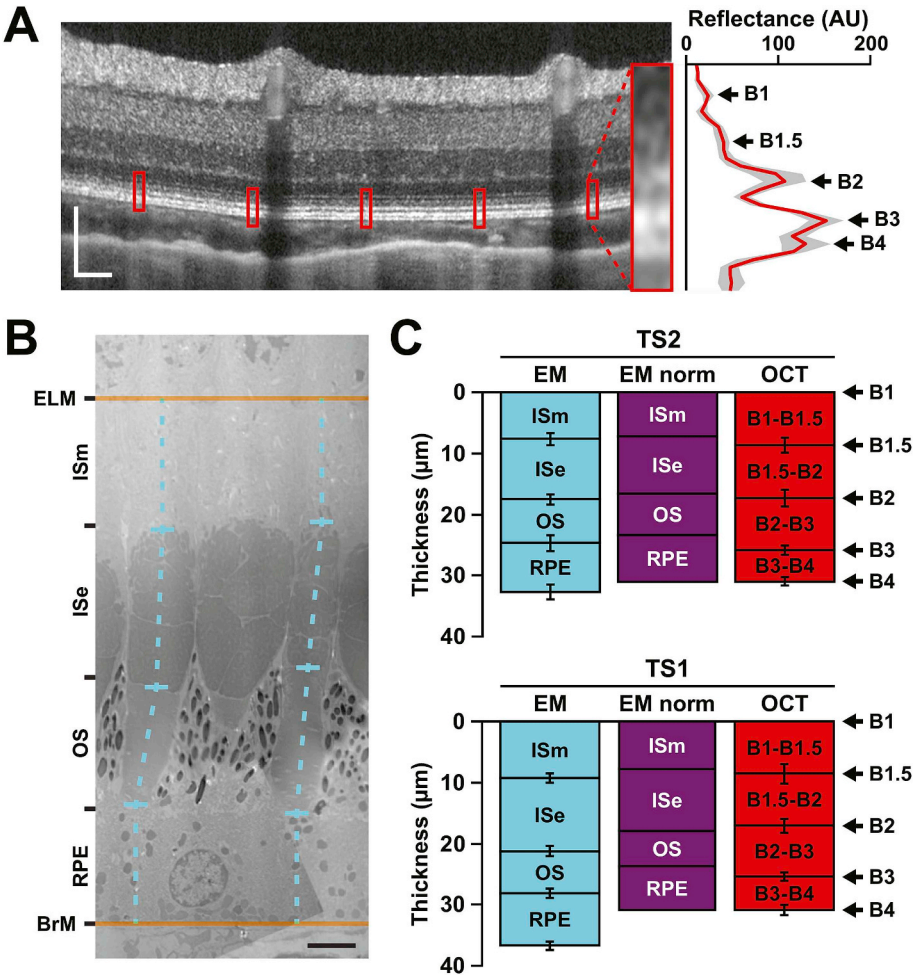

Fig. 6. Intra-animal comparisons of outer retina axial distances in tree shrew retina. (A) Outer retinal peaks in tree shrew (TS2 posterior pole region nasal to the ONH of the left eye) OCT. Image is displayed in logarithmic format while a linear image was used to collect LRPs. *Red boxes* on the OCT represent the locations of the enlarged averaged LRP (*red line*) with 95% confidence internal shading (*gray area*) on the right. One location has been magnified for better visualization of the outer retinal bands (*inset*). Scale bar = 100 μm. (B) Electron micrograph (EM) of tree shrew (TS2 left eye) cones. Axial distances (*dashed cyan lines*) were measured from vertically oriented cones in between the anatomical external limiting membrane (ELM) and Bruch's membrane (BrM). Out-of-plane structures (*e.g.*, the middle cone's outer segment in [B]) were excluded from analysis. ISm: inner segment myoid; ISe: inner segment ellipsoid; OS: outer segment; RPE: retinal pigmented epithelium. Scale bar = 3 μm. (C) Comparison of EM axial distances to OCT peak-to-peak distances in two tree shrew eyes (mean of 10 measurements ± SD). Once the EM distances (*cyan*) between the ELM and BrM were normalized to B1 and B4 to account for axial differences due to tissue processing ("EM norm", *purple*), B1.5 aligns to the anatomical ISm/ISe junction and B2 aligns to the anatomical ISe/OS junction. (For interpretation of the references to color in this figure legend, the reader is referred to the Web version of this article.)

ISe = 9.9 ± 0.8 μm.

4. Discussion

Northern tree shrews are a useful, but under-utilized model for vision science. They possess a nearly cone-exclusive photoreceptor mosaic (Müller and Peichl, 1989), which we have demonstrated can be reliably assessed noninvasively with high-resolution AOSLO. Here we provided an optical characterization of the tree shrew eye, compared these optical data to the photoreceptor mosaic acquired with AOSLO, and, finally, showed intra-animal *in vivo* to *ex vivo* comparisons of cone structure from similar retinal locations *en face* with AOSLO and whole-mount histology, and cross-sectionally with OCT and TEM.

4.1. Optical properties and comparison to humans and mice

There are several approaches to evaluate the optics of the tree shrew eye compared to other species. The change in HORMS as a function of pupil size shown on Fig. 7A reveal that the flatness of the wave aberration in tree shrews falls midway between humans and mice. For any given pupil size, the HORMS of a tree shrew is about 4 times lower than a mouse and about 4 times higher than a human. However, when measured by other criteria, the tree shrew might be considered to have equivalent, or even better optical quality than a human. To have an equivalent HORMS, the pupil sizes for the mouse, tree shrew and human would have to be 2, 3.5 and 6 mm respectively. As such, the blur they experience for vision would be about equal for those pupil sizes. When comparing human and tree shrew MTFs for a 4 mm pupil size (Fig. 7B), the lower contrast in the tree shrew is apparent, but the contrast at the photoreceptor sampling limit in the tree shrew (0.23 at 6 cyc/deg) is about two times better than in the human fovea (0.12 at 60 cyc/deg). By this measure, the tree shrew's optics are better than the human relative to their retinal and visual sampling limits. Finally, owing to the higher numerical aperture of the tree shrew compared to the human, the physical size of the best-focused spot on the tree shrew retina is smaller than for a human with the same pupil size, despite the humans' lower aberrations. This is apparent in the finer scale of the image in cycles/mm in the MTF (Fig. 7B) and also in Fig. 7C, which shows the comparison of PSFs on a common linear spatial scale relative to the photoreceptors. The example PSFs chosen for display were at the 30th, 50th, and 70th percentiles of the HORMS scale in the 74 human subjects (Cheng et al., 2004), and 3rd, 5th, and 7th ranked tree shrews on the HORMS scale. The implication of this is that the ability to resolve fine detail in images taken of the tree shrew retina is better than in a human, even with their native aberrations. With aberrations corrected, the resolution in microns in a tree shrew is more than 3 times better than in a human for the same pupil size.

4.2. Refractive state of normal tree shrews

When measured with streak retinoscopy or other assessment methods, the eyes of small mammals appear to be significantly hyperopic (Glickstein and Millodot, 1970; Hughes, 1977; Mutti et al., 1997; Norton and McBrien, 1992). This is the case for tree shrews; retinoscopy at the juvenile ages examined in this study typically give values of around 7 D hyperopic. A slightly lower value of ~6 D was obtained with a Hartinger coincidence optometer. The Nidek autorefractor used in the present study provided readings of 5.01 ± 1.01 D.

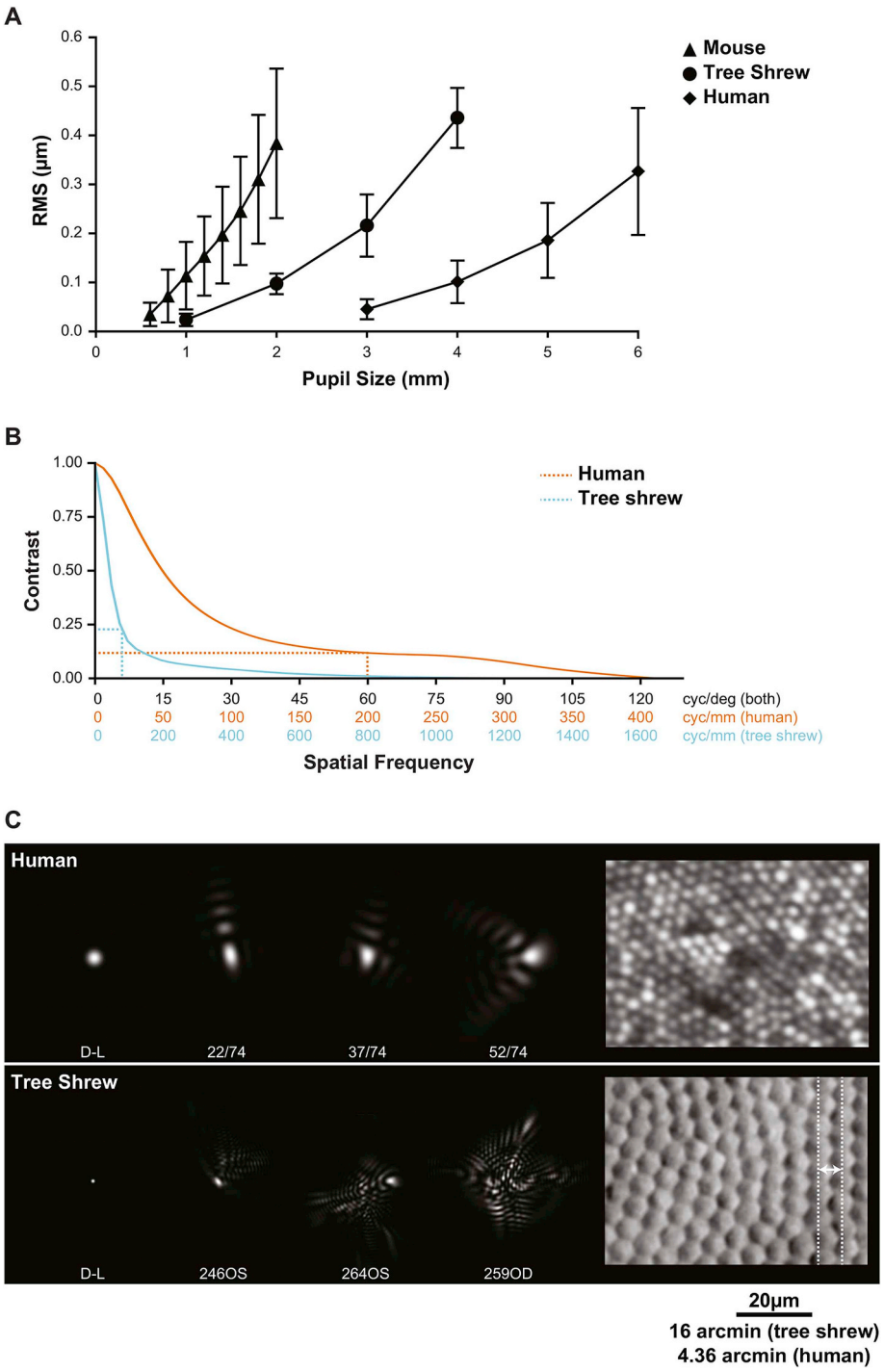

Fig. 7. Interspecies comparison of optics. (A) RMS as a function of pupil size for mouse (Geng et al., 2011), tree shrew and human (Salmon and van de Pol, 2006). (B) Radially-averaged MTF for tree shrews (n = 11 eyes) and humans (n = 74 eyes (Cheng et al., 2004)) for a 4 mm pupil. Dotted lines indicate the spatial frequency cutoff and the corresponding contrast for each species. (C) Comparison of PSFs and cone spacing for tree shrew and human. D–L: diffraction-limited PSF; *dashed lines*: row-to-row separation for tree shrews (6.5 µm). Scale bar = 20 µm.

Glickstein and Millodot (1970) suggested the apparent hyperopia is due to an "error of retinoscopy" that occurs because these instruments measure the location of the optic nerve layer. In the present study, we found evidence of this in the observation of two overlapping spot patterns of different sizes observed in the SHWS images (Supplementary Fig. 2). Using cortical VEPs elicited by checkerboard patterns in combination with trial lenses, Norton et al. (2003) suggested that juvenile tree shrews are nearly emmetropic and that 4.0 D should be subtracted from the autorefractor measured values. The calculated refractive state from the posterior SHWS image agrees well with these corrected values (Table 1), supporting the suggestion that the refractive state of normal juvenile tree shrews is close to emmetropia (slightly hyperopic).

4.3. Limitations and next directions for optical analyses

We provide a comprehensive analysis of the optical properties of the tree shrew eye and some comparison with other species but note that there are limitations in the current study that may guide future

research. First, the optical and anatomical comparisons were made on different animals from different labs. We do not know the extent to which rearing conditions affect the physical and optical characteristics between the two cohorts. For example, institutional differences in husbandry, nutrition, and caging conditions are uncontrolled variables in this study. Second, all optical measurements were made perpendicular to the pupil, along the optical axis of the eye. We did not compute aberrations along the line of sight (an axis connecting the center of the pupil to the area centralis). We collected Shack-Hartmann images along this axis but have not yet devised the tools to properly analyze wavefront aberrations over a highly elliptical pupil. Third, any discussion of the relationship between the optics, retinal sampling characteristics, and visual function should not only consider the photoreceptor sampling, but their connections to downstream neurons and the convergence/divergence of retinal signals. In the human we have every reason to think that signals at the spatial scale of the photoreceptors reach the visual cortex, but, based on receptive fields measured in the lateral geniculate nucleus (Holdefer and Norton, 1995) that does not appear to occur in tree shrews. However, given that the optics are sufficiently good relative to the photoreceptor array, it follows that the optics are also sufficiently good for all neurons downstream of them. In fact, the optical contrast of the retinal image is above 50% at the reported spatial acuity limits of the tree shrew (max 2.5 cyc/deg (Petry et al., 1984)).

4.4. Amenability of tree shrews to noninvasive retinal imaging

As with other small animal models, anesthetized tree shrews require careful monitoring and temperature control during the measurement sessions. None of the animals developed cold-induced cataracts, which have been reported to occur in mice (Bermudez et al., 2011) and can interfere with retinal imaging (Zhou et al., 2012). In this respect, they were similar to the 13-lined ground squirrel, that has extreme cold tolerance owing to its hibernation physiology (Sajdak et al., 2016).

The multiple peaks on confocal AOSLO resulted in difficulty estimating the exact center of each cone for analysis. The non-uniform reflectivity of the cones in the confocal images likely arises because the focused spot in the tree shrew is small relative to the cone and therefore captures more fine details in the scattering and waveguide mode structure in the cones comparable to what is seen in confocal images of large human cones in the periphery (Sulai and Dubra, 2012). So, to reliably identify cones in the tree shrew, we used split-detector AOSLO (Scoles et al., 2014) and the “adaptive filtering and local detection” algorithm (Cunefare et al., 2016). Alternative solutions for traditional confocal AOSLO systems may include temporal averaging (Dubra et al., 2011; Putnam et al., 2010) or larger convolution kernels before local-maximum detection (Li and Roorda, 2007). This illustrates the important point that AO image acquisition, processing, and analysis techniques that work for humans do not necessarily translate to animal subjects.

4.5. In vivo to ex vivo comparisons

The cone density from split-detection AOSLO images are consistent with previous topographical reports in this species of tree shrew (Müller and Peichl, 1989; Petry et al., 1993), with fairly uniform cone density across the horizontal meridian, and a gradient of decreasing density superiorly from the ONH (Fig. 4D). The range of densities from central retinal regions we assessed *in vivo* was 33,366 to 24,489 cones/mm^2 (Fig. 4C), which is also consistent with previous *ex vivo* topographical studies (Müller and Peichl, 1989; Petry et al., 1993). Comparable nasal variability fluctuating within that range was seen in ROIs assessed with AOSLO (Fig. 4A). Similar variability in *ex vivo* topography was thought to be related to variable tissue shrinkage in whole-mounted retina (Petry et al., 1993), but this variability holds true *in vivo* as well. While our AOSLO design affords high lateral resolution, it is limited by a relatively small field-of-view (2° × 2°). Therefore, we were only able to sample narrow 0.2 x 2–3 mm continuous retinal strips in one direction. Since the animals are under anesthesia and must be rotated to image different retinal locations, eye drift from a suboptimal anesthesia plane would disrupt the montage continuation and leave the imaging team lost in retinal space. With the ONH as the only truly unambiguous landmark at this magnification, we could return to the previously imaged location by retracing our steps from the ONH, but this adds a substantial delay in the imaging session (the prolonged anesthesia would be dangerous to the animal). Due to the potentially excessive resolution for these kinds of structural assessments of the cone mosaic, sacrificing resolution for a wider field-of-view would be appropriate for this species to cover more retinal area within the limited time of an imaging session. As mentioned above, the temporal retina was largely inaccessible for *in vivo* retinal imaging in our hands due to our anesthesia nosecone and the anatomy of the tree shrew. The ONH is temporally offset (opposite of humans), and their long nose can inhibit access to the area centralis that is positioned near the temporal ora serrata. With the radial vascular pattern of smaller vessels around this temporal area centralis, there does not seem to be any increase in cone density (Fig. 4D (Müller and Peichl, 1989; Petry et al., 1993);).

Comparing aligned regions equidistant from the ONH revealed similar cone densities *in vivo* (AOSLO) and *ex vivo* (whole-mount) (Fig. 5). As expected, there was variable increase in cone density in the regions assessed from the whole-mounted retina. Grouped by modality, cone density significantly increased in whole-mount ROIs compared to AOSLO ROIs (Fig. 5C). While our AOSLO and whole-mount inter-cell spacing agreed with the 5–6 μm range reported in Müller and Peichl (1989), tissue shrinkage was variable and was often higher in the more peripheral regions compared. While a single shrinkage factor can be derived by averaging the effect seen using intra-animal comparisons (4.5% in this study), shrinkage is likely to have a greater effect towards the edge of whole-mount preparations and away from anchoring retinal structures such as blood vessels. Tissue shrinkage is often assumed to be nominal, however; previous reports derived lateral shrinkage from fresh to fixed tissue ranging from 7 to 25% (Curcio et al., 1987; Kolb and Wang, 1985; Reymond, 1985). The few reports assessing shrinkage from living tissue to fixed tissue report ranges from 14.5 to 29% in the human fovea (Curcio et al., 2011), and anywhere from 0 to 40% in tree shrew retina depending on the fixation method used (Abbott et al., 2009). Additional differences may arise from converting scale from degrees to microns in our *in vivo* analysis, which includes an assumption in sphericity when using a constant retinal magnification factor at each retinal eccentricity. This is an understudied area with respect to direct *in vivo* to *ex vivo* comparisons and will be important for translating scale of images when sub-cellular assessment by histology is necessary.

S-cones did not appear to affect the local geometry of the cone mosaic (Supplementary Fig. 2). A disruption to mosaic regularity may have been expected, as S-cones are reported to be morphologically distinct in many species, including humans (Ahnelt, 1985; Ahnelt et al., 1987; Curcio et al., 1991; Hofer et al., 2005), and S-cone packing in the tree shrew is similar to that in the human retina (Curcio et al., 1991; Martin et al., 2000). The S-cone diameters did not appear to differ in the tree shrew upon histological evaluation (Müller and Peichl, 1989), but this may be confounded by dehydration during fixation. Cone typing using cellular-resolution *in vivo* imaging methods, which has been demonstrated in humans (Hofer et al., 2005; Roorda and Williams, 1999; Sabesan et al., 2015; Zhang et al., 2019), is a potential avenue to investigate this further, as packing geometry of cone types could be assessed before histological manipulation of the tissue, though no structural differences were seen in S-cones compared to L- and M-cones using adaptive optics retinal densitometry in non-human primates (Roorda et al., 2001).

Rod photoreceptors were rarely seen and much smaller (diameter: ~1 μm), but when present and reflective were visible by AOSLO (Fig. 3C). Rod outer segments appear longer, are found closer to the

ELM, and their inner segment mitochondria resemble the more typical elongated structure for mammals compared to cone megamitochondria (Supplementary Fig. 3 (Kühne, 1983)). Other than these qualitative assessments, rods were not included in our analysis.

Advancements in broadband laser sources, dispersion compensation (Cense et al., 2004; Leitgeb et al., 2004; Wojtkowski et al., 2004), and the application of frequency-domain interferometry to OCT (Wojtkowski et al., 2002) has resulted in higher axial resolution, enabling the differentiation of 5 distinct hyperreflective bands in the outer retina of the tree shrew since its initial demonstration (Abbott et al., 2009). Controversy has circled the subcellular attribution of these bands since a comprehensive review of photoreceptor structure lengths from human histology resulted in a model assigning B2 to the ISe (Spaide and Curcio, 2011) and the ellipsoid zone was then adopted as the official nomenclature for this band (Staurenghi et al., 2014). Our results from intra-animal *in vivo* OCT to *ex vivo* TEM comparisons argue in favor of a contribution of the ISm/ISe junction to B1.5 and the IS/OS junction to B2 (Fig. 6C). To our knowledge, this represents the first intra-animal histological evidence for these assignments, which were originally selected (Wojtkowski et al., 2004) due to their theoretical support since the probability of backscattering increases with the change in refractive index. This argument hinges on precise refractive index measurements (which are not yet available for the tree shrew cone) and/or the presence of a small gap between the ISe and the OS containing interstitial fluid of relatively low refractive index, the existence of which is questionable (potentially arising from histologic artifact) (Burgoyne et al., 2015; Hoang et al., 2002), and not seen in our TEM results. Importantly, our results also support mitochondria as a source of reflectivity (Fig. 6C), as has been shown in many experimental and clinical studies (Litts et al., 2018; Wilson et al., 2007). Due to the axial resolution of the Bioptigen system ($\sim$1.37 μm in tissue; $n = 1.336$ (Izatt and Choma, 2008)), we can conclude that B2 cannot come from the entire ellipsoid region in the tree shrew, as the size of the local maxima of B2 at FWHM is only 33% of the axial distance as the ISe seen in TEM. It is likely that the megamitochondria of tree shrew cones (Supplementary Fig. 3) are all weakly reflective, giving rise to B1.5 (Fig. 6A). The focusing power of mitochondria toward the outer ISe was recently modeled in the cones of ground squirrels (Li et al., 2017); however, the distinction between whether light is focused and scattered at the outer EZ or IS/OS will not be solvable with axial distance comparisons reliant on *ex vivo* ultrastructure unless histological confounds can be eliminated. Alternative *in vivo* approaches include using reflective nano-particles targeted to specific organelles (de la Zerda et al., 2015; Hayashi et al., 2009; Zagaynova et al., 2008).

Potential confounds exist for both *in vivo* and *ex vivo* measurements. Non-linear tissue shrinkage is a potential confound in all studies attempting to correlate subcellular structures to OCT signals, as water-rich compartments between B1-4 (*i.e.,* ISm, RPE) may change more than compartments comprising convoluted cristae of lipid membranes (*i.e.,* ISe, OS). Scaling the measurements of B1-4 linearly may result in an over- and under-estimation of the lengths of water-rich and lipid-rich components, respectively. Moreover, the z- (axial) component of the pixel size on OCT is inversely related to refractive index, which varies slightly for each subcellular compartment (by $\sim$5%) (Sidman, 1957) creating a potential source of error since a single refractive index was used to estimate pixel size in this study. However, due to the relatively short length of the compartments between B1-4, this error (on the order of < 1 μm) would not likely result in a misattribution of a hyperreflective band. Caution should be exercised however, if the retina were scaled linearly using the nerve fiber layer and the RPE as boundaries, as this would increase the likelihood of over-estimating thickness of nuclear layers due to their relatively lower refractive index.

5. Conclusions

The present study provides new data that support the use of tree shrews as an animal model intermediate between rodents and primates. Tree shrews have excellent optics and are nearly emmetropic. We found that they are amenable to noninvasive study of retinal structures including investigation of cone mosaics and subcellular sources of reflectivity in the retina. They can be used to study living cones and have potential for modeling cone disorders with longitudinal follow-up. Thus, the tree shrew strikes a balance between practicality and relevance that is warranted as a complementary model for vision science research. To this end, any raw data generated in this study would be happily provided upon request with the corresponding author.

Disclosures

B.S. Sajdak, none; A.E. Salmon, none; J.A. Cava, none; K.P. Allen, none; S. Freling, none; R. Ramamirtham, none; T.T. Norton, none; A. Roorda, Patent (USPTO#7118216) assigned to the University of Houston and the University of Rochester, which is currently licensed to Boston Micromachines Corp (Watertown, MA). Both he and the company stand to gain financially from the publication of these results; J. Carroll, Consultant: Translational Imaging Innovations.

Grant information

Research reported in this manuscript was supported in part by the National Eye Institute of the National Institutes of Health (NIH, Bethesda, MD, USA) under award numbers U24EY029891, R01EY005922, P30EY001931, P30EY003039, T32EY014537, and U01EY025477. This research was conducted in part in a facility constructed with support from Research Facilities Improvement Program Grant Number C06RR016511 from the National Center for Research Resources, NIH. The content is solely the responsibility of the authors and does not necessarily represent the official views of the NIH. Additional support from the Alcon Research Institute.

Acknowledgements

The authors thank Christine Skumatz, Tiffany Butler, Lisa King, and the Biomedical Resource Center at MCW for their contributions to tree shrew care, Brian Samuels and David Fitzpatrick for helpful discussion on working with tree shrews, Ross Collery for whole-mount protocol assistance, Brian Cohn for his enthusiastic assistance with the 'Retina' topography package, Clive Wells and Rob Goodwin for help preparing TEM samples, Jeremy Nathans for sharing opsin antibodies, Suresh Kumar for performing confocal microscopy scanning of whole-mount retinas, Katie Litts for valuable discussion regarding OCT reflectivity, Rob Cooper for developing and supporting the AO analysis software, Alfredo Dubra for developing the AOSLO optical design, and software for AO control, image acquisition and image registration, Nripun Sredar for AOSLO assembly and maintenance, Dan Lipinski for sharing his cSLO, and John T. Siegwart, Jr. for assistance with wavefront measurements in awake tree shrews.

Appendix A. Supplementary data

Supplementary data to this article can be found online at https://doi.org/10.1016/j.exer.2019.05.023.

References

Abbott, C.J., Grünert, U., Pianta, M.J., McBrien, N.A., 2011. Retinal thinning in tree shrews with induced high myopia: optical coherence tomography and histological assessment. Vision Res. 51, 376–385. https://doi.org/10.1016/j.visres.2010.12.005.

Abbott, C.J., McBrien, N.A., U, G., Pianta, M.J., 2009. Relationship of the optical coherence tomography signal to underlying retinal histology in the tree shrew (*Tupaia belangeri*). Investigative Ophthalmol. Visual Sci. 50, 414–423. https://doi.org/10.1167/iovs.07-1197.

Ahnelt, P.K., 1985. Characterization of the color related receptor mosaic in the ground squirrel retina. Vision Res. 25, 1557–1567. https://doi.org/10.1016/0042-6989(85)90126-9.

Ahnelt, P.K., Kolb, H., Pflug, R., 1987. Identification of a subtype of cone photoreceptor, likely to be blue sensitive, in the human retina. J. Comp. Neurol. 255, 18–34. https://doi.org/10.1002/cne.902550103.

Beier, C., Palanker, D., Sher, A., 2018. Stereotyped synaptic connectivity is restored during circuit repair in the adult mammalian retina. Curr. Biol. 28, 1818–1824. https://doi.org/10.1016/j.cub.2018.04.063.

Beltran, W.A., Cideciyan, A.V., Guziewicz, K.E., Iwabe, S., Swider, M., Scott, E.M., Savina, S.V., Ruthel, G., Stefano, F., Zhang, L., Zorger, R., Sumaroka, A., Jacobson, S.G., Aguirre, G.D., 2014. Canine retina has a primate fovea-like bouquet of cone photoreceptors which is affected by inherited macular degenerations. PLoS One 9, e90390. https://doi.org/10.1371/journal.pone.0090390.

Bermudez, M.A., Vicente, A.F., Romero, M.C., Arcos, M.D., Abalo, J.M., Gonzalez, F., 2011. Time course of cold cataract development in anesthetized mice. Curr. Eye Res. 36, 278–284. https://doi.org/10.3109/02713683.2010.542868.

Bobu, C., Craft, C.M., Masson-Pevet, M., Hicks, D., 2006. Photoreceptor organization and rhythmic phagocytosis in the nile rat Arvicanthis ansorgei: a novel diurnal rodent model for the study of cone pathophysiology. Investigative Ophthalmol. Visual Sci. 47, 3109–3118. https://doi.org/10.1167/iovs.05-1397.

Burgoyne, T., Meschede, I.P., Burden, J.J., Bailly, M., Seabra, M.C., Futter, C.E., 2015. Rod disc renewal occurs by evagination of the ciliary plasma membrane that makes cadherin-based contacts with the inner segment. Proc. Natl. Acad. Sci. U. S. A 112, 15922–15927. https://doi.org/10.1073/pnas.1509285113.

Callahan, T.L., Petry, H.M., 2000. Psychophysical measurement of temporal modulation sensitivity in the tree shrew (*Tupaia belangeri*). Vision Res. 40, 455–458. https://doi.org/10.1016/S0042-6989(99)00194-7.

Cense, B., Nassif, N., Chen, T., Pierce, M., Yun, S.-H., Park, B., Bouma, B., Tearney, G., de Boer, J., 2004. Ultrahigh-resolution high-speed retinal imaging using spectral-domain optical coherence tomography. Opt. Express 12, 2435–2447. https://doi.org/10.1364/OPEX.12.002435.

Chen, M., Cooper, R.F., Han, G.K., Gee, J., Brainard, D.H., Morgan, J.I., 2016. Multimodal automatic montaging of adaptive optics retinal images. Biomed. Opt. Express 7, 4899–4918. https://doi.org/10.1364/BOE.7.004899.

Cheng, H., Barnett, J.K., Vilupuru, A.S., Marsack, J.D., Kasthurirangan, S., Applegate, R.A., Roorda, A., 2004. A population study on changes in wave aberrations with accommodation. J. Vision 4, 272–280. https://doi.org/10.1167/4.4.3.

Cohn, B.A., Collin, S.P., Wainwright, P.C., Schmitz, L., 2015. Retinal topography maps in R: new tools for the analysis and visualization of spatial retinal data. J. Vision 15, 19. https://doi.org/10.1167/15.9.19.

Cooper, R.F., Dubis, A.M., Pavaskar, A., Rha, J., Dubra, A., Carroll, J., 2011. Spatial and temporal variation of rod photoreceptor reflectance in the human retina. Biomed. Opt. Express 2, 2577–2589. https://doi.org/10.1364/BOE.2.002577.

Cooper, R.F., Lombardo, M., Carroll, J., Sloan, K.R., Lombardo, G., 2016. Methods for investigating the local spatial anisotropy and the preferred orientation of cones in adaptive optics retinal images. Visual Neurosci. 33, E005. https://doi.org/10.1017/S0952523816000018.

Cunefare, D., Cooper, R.F., Higgins, B., Katz, D.F., Dubra, A., Carroll, J., Farsiu, S., 2016. Automatic detection of cone photoreceptors in split detector adaptive optics scanning light ophthalmoscope images. Biomed. Opt. Express 7, 2036–2050. https://doi.org/10.1364/BOE.7.002036.

Curcio, C.A., Allen, K.A., Sloan, K.R., Lerea, C.L., Hurley, J.B., Klock, I.B., Milam, A.H., 1991. Distribution and morphology of human cone photoreceptors stained with anti-blue opsin. J. Comp. Neurol. 312, 610–624. https://doi.org/10.1002/cne.903120411.

Curcio, C.A., Messinger, J.D., Sloan, K.R., Mitra, A., McGwin, G., Spaide, R.F., 2011. Human chorioretinal layer thicknesses measured in macula-wide, high-resolution histologic sections. Investigative Ophthalmol. Visual Sci. 52, 3943–3954. https://doi.org/10.1167/iovs.10-6377.

Curcio, C.A., Packer, O., Kalina, R.E., 1987. A whole mount method for sequential analysis of photoreceptor and ganglion cell topography in a single retina. Vision Res. 27, 9–15. https://doi.org/10.1016/0042-6989(87)90137-4.

de la Zerda, A., Prabhulkar, S., Perez, V.L., Ruggeri, M., Paranjape, A.S., Habte, F., Gambhir, S.S., Awdeh, R.M., 2015. Optical coherence contrast imaging using gold nanorods in living mice eyes. Clin. Exp. Ophthalmol. 43, 358–366. https://doi.org/10.1111/ceo.12299.

Dubra, A., Harvey, Z., 2010. Registration of 2D images from fast scanning ophthalmic instruments. In: Fischer, B., Dawant, B., Lorenz, C. (Eds.), Biomedical Image Registration, 1 ed. Springer-Verlag, Berlin, pp. 60–71. https://doi.org/10.1007/978-3-642-14366-3_6.

Dubra, A., Sulai, Y., Norris, J.L., Cooper, R.F., Dubis, A.M., Williams, D.R., Carroll, J., 2011. Noninvasive imaging of the human rod photoreceptor mosaic using a confocal adaptive optics scanning ophthalmoscope. Biomed. Opt. Express 2, 1864–1876. https://doi.org/10.1364/BOE.2.001864.

Emmons, L.H., 2000. Tupai. A Field Study of Bornean Treeshrews. University of California Press, Berkely, California.

Erchova, I., Tumlinson, A.R., Fergusson, J., White, N., Drexler, W., Sengpiel, F., Morgan, J.E., 2018. Optophysiological characterisation of inner retina responses with high-resolution optical coherence tomography. Sci. Rep. 8, 1813. https://doi.org/10.1038/s41598-018-19975-x.

Gawne, T.J., Ward, A.H., Norton, T.T., 2018. Juvenile tree shrews do not maintain emmetropia in narrow-band blue light. Optom. Vision Sci. 95, 911–920. https://doi.org/10.1097/OPX.0000000000001283.

Geng, Y., Schery, L.A., Sharma, R., Dubra, A., Ahmad, K., Libby, R.T., Williams, D.R., 2011. Optical properties of the mouse eye. Biomed. Opt. Express 2, 717–738. https://doi.org/10.1364/BOE.2.000717.

Glickstein, M., Millodot, M., 1970. Retinoscopy and eye size. Science 168, 605–606. https://doi.org/10.1126/science.168.3931.605.

Hayashi, A., Naseri, A., Pennesi, M.E., de Juan, E.J., 2009. Subretinal delivery of immunoglobulin G with gold nanoparticles in the rabbit eye. Jpn. J. Ophthalmol. 53, 249–256. https://doi.org/10.1007/s10384-009-0655-x.

Hendrickson, A., Hicks, D., 2002. Distribution and density of medium- and short-wavelength selective cones in the domestic pig retina. Exp. Eye Res. 74, 435–444. https://doi.org/10.1006/exer.2002.1181.

Hoang, Q.V., Linsenmeier, R.A., Chung, C.K., Curcio, C.A., 2002. Photoreceptor inner segments in monkey and human retina: mitochondrial density, optics, and regional variation. Visual Neurosci. 19, 395–407. https://doi.org/10.1017/S0952523802194028.

Hofer, H., Carroll, J., Neitz, J., Neitz, M., Williams, D.R., 2005. Organization of the human trichromatic cone mosaic. J. Neurosci. 25, 9669–9679. https://doi.org/10.1523/JNEUROSCI.2414-05.2005.

Holdefer, R.N., Norton, T.T., 1995. Laminar organization of receptive field properties in the dorsal lateral geniculate nucleus of the tree shrew (*Tupaiaglis belangeri*). J. Comp. Neurol. 358, 401–413. https://doi.org/10.1002/cne.903580307.

Hughes, A., 1977. The topography of vision in animals with contrasting life styles. In: Crescitelli, F. (Ed.), Handbook of Sensory Physiology. Springer, Berlin, pp. 614–642.

Hughes, A., 1979. A useful table of reduced schematic eyes for vertebrates which includes computed longitudinal chromatic aberrations. Vision Res. 19, 1273–1275. https://doi.org/10.1016/0042-6989(79)90195-0.

Huibers, P.D.T., 1997. Models for the wavelength dependence of the index of refraction of water. Appl. Opt. 36, 3785–3787. https://doi.org/10.1364/AO.36.003785.

Izatt, J.A., Choma, M.A., 2008. Theory of optical coherence tomography. In: Drexler, W., Fujimoto, J.G. (Eds.), Optical Coherence Tomography: Technology and Applications, 1 ed. Springer Berlin Heidelberg, Berlin, Heidelberg, pp. 47–72. https://doi.org/10.1007/978-3-319-06419-2_3.

Jacobs, G.H., Neitz, J., 1986. Spectral mechanisms and color vision in the tree shrew (*Tupaia belangeri*). Vision Res. 26, 292–298. https://doi.org/10.1016/0042-6989(86)90026-X.

Kaas, J.H., Hall, W.C., Killackey, H., Diamond, I.T., 1972. Visual cortex of the tree shrew (Tupaia glis): architectonic subdivisions and representations of the visual field. Brain Res. 42, 491–496. https://doi.org/10.1016/0006-8993(72)90548-3.

Kaplan, H.J., Wang, W., Dean, D.C., 2017. Restoration of cone photoreceptor function in retinitis pigmentosa. Trans. Vision Sci. Technol. 6, 1–5. https://doi.org/10.1167/tvst.6.5.5.

Kiser, P.D., Zhang, J., Sharma, A., Angueyra, J.M., Kolesnikov, A.V., Badiee, M., Tochtrop, G.P., Kinoshita, J., Peachey, N.S., Li, W., Kefalov, V.J., Palczewski, K., 2018. Retinoid isomerase inhibitors impair but do not block mammalian cone photoreceptor function. J. Gen. Physiol. 150, 571–590. https://doi.org/10.1085/jgp.201711815.

Knabe, W., Skatchkov, S., Kuhn, H.J., 1997. Lens mitochondria" in the retinal cones of the tree-shrew *Tupaia belangeri*. Vision Res. 37, 267–271. https://doi.org/10.1016/S0042-6989(96)00199-X.

Kolb, H., Wang, H.H., 1985. The distribution of photoreceptors, dopaminergic amacrine cells and ganglion cells in the retina of the North American opossum (*Didelphis virginiana*). Vision Res. 25, 1207–1221. https://doi.org/10.1016/0042-6989(85)90035-5.

Kostic, C., Arsenijevic, Y., 2016. Animal modelling for inherited central vision loss. J. Pathol. 238, 300–310. https://doi.org/10.1002/path.4641.

Kryger, Z., Galli-Resta, L., Jacobs, G.H., Reese, B.E., 1998. The topography of rod and cone photoreceptors in the retina of the ground squirrel. Visual Neurosci. 15, 685–691. https://doi.org/10.1017/S0952523898154081.

Kühne, J.H., 1983. Rod receptors in the retina of *Tupaia belangeri*. Anat. Embryol. 167, 95–102. https://doi.org/10.1007/BF00304603.

Kuwabara, T., 1975. Cytologic changes of the retina and pigment epithelium during hibernation. Investigative Ophthalmol. 14, 457–467.

Lee, K.S., Huang, X., Fitzpatrick, D., 2016. Topology of ON and OFF inputs in visual cortex enables an invariant columnar architecture. Nature 533, 90–94. https://doi.org/10.1038/nature17941.

Leitgeb, R.A., Drexler, W., Unterhuber, A., Hermann, B., Bajraszewski, T., Le, T., Stingl, A., Fercher, A.F., 2004. Ultrahigh resolution Fourier domain optical coherence tomography. Opt. Express 12, 2156–2165. https://doi.org/10.1364/OPEX.12.002156.

Li, K.Y., Roorda, A., 2007. Automated identification of cone photoreceptors in adaptive optics retinal images. J. Opt. Soc. Am. A Opt. Image Sci. Vision 24, 1358–1363. https://doi.org/10.1364/JOSAA.24.001358.

Li, W., Ball, J., Chen, S., 2017. Cone mitochondria enhance light transmission. Investigative Ophthalmol. Visual Sci. 58 E-Abstract: 1037.

Liang, J., Williams, D.R., 1997. Aberrations and retinal image quality of the normal human eye. J. Opt. Soc. Am. A Opt. Image Sci. Vision 14, 2873–2883. https://doi.org/10.1364/JOSAA.14.002873.

Link, B.A., Collery, R.F., 2015. Zebrafish models of retinal disease. Ann. Rev. Vision Sci. 1, 125–153. https://doi.org/10.1146/annurev-vision-082114-035717.

Litts, K.M., Zhang, Y., Freund, K.B., Curcio, C.A., 2018. Optical coherence tomography

and histology of age-related macular degeneration support mitochondria as reflectivity sources. Retina 38, 445–461. https://doi.org/10.1097/IAE.0000000000001946.
Luan, Y., Ou, J., Kunze, V.P., Qiao, F., Wang, Y., Wei, L., Li, W., Xie, Z., 2017. Integrated transcriptomic and metabolomic analysis reveals adaptive changes of hibernating retinas. J. Cell. Physiol. https://doi.org/10.1002/jcp.26030.
Lund, J.S., Fitzpatrick, D., Humphrey, A.L., 1985. The striate visual cortex of the tree shrew, Cerebral cortex. Visual Cortex 3, 157–205 Plenum Press, New York, NY.
Lundstrom, L., Unsbo, P., 2007. Transformation of Zernike coefficients: scaled, translated, and rotated wavefronts with circular and elliptical pupils. J. Opt. Soc. Am.. A Opt. Image Sci. Vision 24, 569–577. https://doi.org/10.1364/JOSAA.24.000569.
Martin, P.R., Grünert, U., Chan, T.L., Bumsted, K., 2000. Spatial order in short-wavelength-sensitive cone photoreceptors: a comparative study of the primate retina. J. Opt. Soc. Am.. A Opt. Image Sci. Vision 17, 557–579. https://doi.org/10.1364/JOSAA.17.000557.
McFadden, S.A., Howlett, M.H., Mertz, J.R., 2004. Retinoic acid signals the direction of ocular elongation in the Guinea pig eye. Vision Res. 44, 643–653. https://doi.org/10.1016/j.visres.2003.11.002.
Mehta, B., Snellman, J., Chen, S., Li, W., Zenisek, D., 2013. Synaptic ribbons influence the size and frequency of miniature-like evoked postsynaptic currents. Neuron 77, 516–527. https://doi.org/10.1016/j.neuron.2012.11.024.
Merriman, D.K., Sajdak, B.S., Li, W., Jones, B.W., 2016. Seasonal and post-trauma remodeling in cone-dominant ground squirrel retina. Exp. Eye Res. 150, 90–105. https://doi.org/10.1016/j.exer.2016.01.011.
Müller, B., Peichl, L., 1989. Topography of cones and rods in the tree shrew retina. J. Comp. Neurol. 282, 581–594. https://doi.org/10.1002/cne.902820409.
Mustafar, F., Harvey, M.A., Khani, A., Arató, J., Rainer, G., 2018. Divergent solutions to visual problem solving across mammalian species. eNeuro 5 e0167-0118.2018. https://doi.org/10.1523/ENEURO.0167-18.2018.
Mustafi, D., Kevany, B.M., Bai, X., Golczak, M., Adams, M.D., Wynshaw-Boris, A., Palczewski, K., 2016. Transcriptome analysis reveals rod/cone photoreceptor specific signatures across mammalian retinas. Hum. Mol. Genet. 25, 4376–4388. https://doi.org/10.1093/hmg/ddw268.
Mutti, D.O., Ver Hoeve, J.N., Zadnik, K., Murphy, C.J., 1997. The artifact of retinoscopy revisited: comparison of refractive error measured by retinoscopy and visual evoked potential in the rat. Optom. Vision Sci. 74, 483–488. https://doi.org/10.1097/00006324-199707000-00014.
Norton, T.T., Amedo, A.O., Siegwart Jr., J.T., 2010. The effect of age on compensation for a negative lens and recovery from lens-induced myopia in tree shrews (*Tupaia glis belangeri*). Vision Res. 50, 564–576. https://doi.org/10.1016/j.visres.2009.12.014.
Norton, T.T., McBrien, N.A., 1992. Normal development of refractive state and ocular component dimensions in the tree shrew (*Tupaia belangeri*). Vision Res. 32, 833–842. https://doi.org/10.1016/0042-6989(92)90026-F.
Norton, T.T., Siegwart Jr., J.T., Amedo, A.O., 2006. Effectiveness of hyperopic defocus, minimal defocus, or myopic defocus in competition with a myopiagenic stimulus in tree shrew eyes. Investigative Ophthalmol. Visual Sci. 47, 4687–4699. https://doi.org/10.1167/iovs.05-1369.
Norton, T.T., Wu, W.W., Siegwart Jr., J.T., 2003. Refractive state of tree shrew eyes measured with cortical visual evoked potentials. Optom. Vision Sci. 80, 623–631. https://doi.org/10.1097/00006324-200309000-00006.
Peichl, L., Gonzalez-Soriano, J., 1994. Morphological types of horizontal cell in rodent retinae: a comparison of rat, mouse, gerbil, and Guinea pig. Visual Neurosci. 11, 501–517. https://doi.org/10.1017/S095252380000242X.
Petry, H.M., Erichsen, J.T., Szél, A., 1993. Immunocytochemical identification of photoreceptor populations in the tree shrew retina. Brain Res. 616, 344–350. https://doi.org/10.1016/0006-8993(93)90230-K.
Petry, H.M., Fox, R., Casagrande, V.A., 1984. Spatial contrast sensitivity of the tree shrew. Vision Res. 24, 1037–1042. https://doi.org/10.1016/0042-6989(84)90080-4.
Porter, J., Guirao, A., Cox, I.G., Williams, D.R., 2001. Monochromatic aberrations of the human eye in a large population. J. Opt. Soc. Am. A Opt. Image Sci. Vision 18, 1793–1803. https://doi.org/10.1364/JOSAA.18.001793.
Putnam, N.M., Hammer, D.X., Zhang, Y., Merino, D., Roorda, A., 2010. Modeling the foveal cone mosaic imaged with adaptive optics scanning laser ophthalmoscopy. Opt. Express 18, 24902–24916. https://doi.org/10.1364/OE.18.024902.
Quan, X., Fry, E.S., 1995. Empirical equation for the index of refraction of seawater. Appl. Opt. 34, 3477–3480. https://doi.org/10.1364/AO.34.003477.
Remé, C.E., Young, R.W., 1977. The effects of hibernation on cone visual cells in the ground squirrel. Investigative Ophthalmol. Visual Sci. 16, 815–840.
Reymond, L., 1985. Spatial visual acuity of the eagle *Aquila audax*: a behavioural, optical and anatomical investigation. Vision Res. 25, 1477–1491. https://doi.org/10.1016/0042-6989(85)90226-3.
Rodieck, R.W., 1991. The density recovery profile: a method for the analysis of points in the plane applicable to retinal studies. Visual Neurosci. 6, 95–111. https://doi.org/10.1017/S095252380001049X.
Roorda, A., Metha, A.B., Lennie, P., Williams, D.R., 2001. Packing arrangement of the three cone classes in primate retina. Vision Res. 41, 1291–1306. https://doi.org/10.1016/S0042-6989(01)00043-8.
Roorda, A., Williams, D.R., 1999. The arrangement of the three cone classes in the living human eye. Nature (London) 397, 520–522. https://doi.org/10.1038/17383.
Sabesan, R., Hofer, H., Roorda, A., 2015. Characterizing the human cone photoreceptor mosaic via dynamic photopigment densitometry. PLoS One 10, e0144891. https://doi.org/10.1371/journal.pone.0144891.
Sajdak, B., Sulai, Y.N., Langlo, C.S., Luna, G., Fisher, S.K., Merriman, D.K., Dubra, A., 2016. Noninvasive imaging of the thirteen-lined ground squirrel photoreceptor mosaic. Visual Neurosci. 33. e003. https://doi.org/10.1017/S0952523815000346.
Sajdak, B.S., Bell, B.A., Lewis, T.R., Luna, G., Cornwell, G.S., Fisher, S.K., Merriman, D.K., Carroll, J., 2018. Assessment of outer retinal remodeling in the hibernating 13-lined ground squirrel. Investigative Ophthalmol. Visual Sci. 59, 2538–2547. https://doi.org/10.1167/iovs.17-23120.
Salmon, A.E., Cooper, R.F., Langlo, C.S., Baghaie, A., Dubra, A., Carroll, J., 2017. An automated reference frame selection (ARFS) algorithm for cone imaging with adaptive optics scanning light ophthalmoscopy. Trans. Vision Sci. Technol. 6, 9. https://doi.org/10.1167/tvst.6.2.9.
Salmon, T.O., van de Pol, C., 2006. Normal-eye Zernike coefficients and root-mean-square wavefront errors. J. Refract. Surg. 32, 2064–2074. https://doi.org/10.1016/j.jcrs.2006.07.022.
Samorajski, T., Ordy, J.M., Keefe, J.R., 1966. Structural organization of the retina in the tree shrew (*Tupaia glis*). J. Cell Biol. 28, 489–504. https://doi.org/10.1083/jcb.28.3.489.
Samuels, B.C., Siegwart, J.T., Zhan, W., Hethcox, L., Chimento, M., Whitley, R., Downs, J.C., Girkin, C.A., 2018. A novel tree shrew (*Tupaia belangeri*) model of glaucoma. Investigative Ophthalmol. Visual Sci. 59, 3136–3143. https://doi.org/10.1167/iovs.18-24261.
Schneider, C.A., Rasband, W.S., Eliceiri, K.W., 2012. NIH image to ImageJ: 25 years of image analysis. Nat. Methods 9, 671–675. https://doi.org/10.1038/nmeth.2089.
Scoles, D., Sulai, Y.N., Langlo, C.S., Fishman, G.A., Curcio, C.A., Carroll, J., Dubra, A., 2014. In vivo imaging of human cone photoreceptor inner segments. Investigative Ophthalmol. Visual Sci. 55, 4244–4251. https://doi.org/10.1167/iovs.14-14542.
Sesma, M.A., Casagrande, V.A., Kaas, J.H., 1984. Cortical connections of area 17 in tree shrews. J. Comp. Neurol. 230, 337–351. https://doi.org/10.1002/cne.902300303.
Sidman, R.L., 1957. The structure and concentration of solids in photoreceptor cells studied by refractometry and interference microscopy. J. Biophys. Biochem. Cytol. 3, 15–30. https://doi.org/10.1083/jcb.3.1.15.
Siegwart Jr., J.T., Norton, T.T., 1994. Goggles for controlling the visual environment of small animals. Lab. Anim. Sci. 44, 292–294.
Slijkerman, R.W., Song, F., Astuti, G.D., Huynen, M.A., van Wijk, E., Stieger, K., Collin, R.W., 2015. The pros and cons of vertebrate animal models for functional and therapeutic research on inherited retinal dystrophies. Prog. Retin. Eye Res. 48, 137–159. https://doi.org/10.1016/j.preteyeres.2015.04.004.
Spaide, R.F., Curcio, C.A., 2011. Anatomical correlates to the bands seen in the outer retina by optical coherence tomography: literature review and model. Retina 31, 1609–1619. https://doi.org/10.1097/IAE.0b013e3182247535.
Staurenghi, G., Sadda, S., Chakravarthy, U., Spaide, R.F., Panel, I.O., 2014. Proposed lexicon for anatomic landmarks in normal posterior segment spectral-domain optical coherence tomography: the IN•OCT consensus. Ophthalmology 121, 1572–1578. https://doi.org/10.1016/j.ophtha.2014.02.023s.
Sulai, Y.N., Dubra, A., 2012. Adaptive optics scanning ophthalmoscopy with annular pupils. Biomed. Opt. Express 3, 1647–1661. https://doi.org/10.1364/BOE.3.001647.
Thévenaz, P., Ruttimann, U.E., Unser, M., 1998. A pyramid approach to subpixel registration based on intensity. IEEE. Trans. Image. Process 7, 27–41. https://doi.org/10.1109/83.650848.
Thibos, L.N., Applegate, R.A., Schwiegerling, J.T., Webb, R., 2002. Standards for reporting the optical aberrations of eyes. J. Refract. Surg. 18, S652–S660. https://doi.org/10.3928/1081-597X-20020901-30.
Usrey, W.M., Muly, E.C., Fitzpatrick, D., 1992. Lateral geniculate projections to the superficial layers of visual cortex in the tree shrew. J. Comp. Neurol. 319, 159–171. https://doi.org/10.1002/cne.903190113.
Wilk, M.A., Huckenpahler, A.L., Collery, R.F., Link, B.A., Carroll, J., 2017. The effect of retinal melanin on optical coherence tomography images. Trans. Vision Sci. Technol. 6, 8. https://doi.org/10.1167/tvst.6.2.8.
Wilson, J.D., Cottrell, W.J., Foster, T.H., 2007. Index-of-refraction-dependent subcellular light scattering observed with organelle-specific dyes. J. Biomed. Opt. 12, 014010. https://doi.org/10.1117/1.2437765.
Wisely, C.E., Sayed, J.A., Tamez, H., Zelinka, C.P., Abdel-Rahman, M.H., Discher, A.J., Cebulla, C.M., 2017. The chick eye in vision research: an excellent model for the study of ocular disease. Prog. Retin. Eye Res. 61, 72–97. https://doi.org/10.1016/j.preteyeres.2017.06.004.
Wojtkowski, M., Leitgeb, R., Kowalczyk, A., Bajraszewski, T., Fercher, A.F., 2002. In vivo human retinal imaging by Fourier domain optical coherence tomography. J. Biomed. Opt. 7, 457–463. https://doi.org/10.1117/1.1482379.
Wojtkowski, M., Srinivasan, V., Ko, T., Fujimoto, J., Kowalczyk, A., Duker, J., 2004. Ultrahigh-resolution, high-speed, Fourier domain optical coherence tomography and methods for dispersion compensation. Opt. Express 12, 2404–2422. https://doi.org/10.1364/OPEX.12.002404.
Zagaynova, E.V., Shirmanova, M.V., Kirillin, M.Y., Khlebtsov, B.N., Orlova, A.G., Balalaeva, I.V., Sirotkina, M.A., Bugrova, M.L., Agrba, P.D., Kamensky, V.A., 2008. Contrasting properties of gold nanoparticles for optical coherence tomography: phantom, in vivo studies and Monte Carlo simulation. Phys. Med. Biol. 53, 4995–5009. https://doi.org/10.1088/0031-9155/53/18/010.
Zhang, F., Kurokawa, K., Lassoued, A., Crowell, J.A., Miller, D.T., 2019. Cone photoreceptor classification in the living human eye from photostimulation-induced phase dynamics. Proc. Natl. Acad. Sci. U.S.A 116, 7951–7958. https://doi.org/10.1073/pnas.1816360116.
Zhou, X., Bedggood, P., Metha, A., 2012. Limitations to adaptive optics image quality in rodent eyes. Biomed. Opt. Express 3, 1811–1824. https://doi.org/10.1364/BOE.3.001811.